An Effective Space-Borne ISAR High-Resolution Imaging Approach for Satellite On-Orbit Based on Minimum Entropy Optimization

Yifei Liu, Weidong Yu, *Member, IEEE*, Shenghui Yang, and Shiqiang Li

***Abstract*—The space situational awareness program places great significance on obtaining high-resolution images of satellite in space orbit. By utilizing space-borne inverse synthetic aperture radar (SBISAR) can achieve high-resolution imaging of observed satellite (OS) on-orbit especially in geosynchronous orbit (GEO). However, the complex and nonuniform relative motion of the OS on-orbit and SBISAR produces 2-D spatial variant phase errors, which has a high-order form during long coherent processing intervals. Up to now, the imaging problem of SBISAR has not been effectively tackled. In this work, a novel method to compensate for the 2-D spatial variant phase errors for SBISAR imaging based on minimum entropy and quasi-Newton's method is proposed. First, the geometric model that considers the relative motion state of SBISAR and the OS on-orbit is established and the optimal observation time period is determined. Second, we propose the echo signal model for the satellite on-orbit and deduce the specific form of the high-order spatial variant phase errors. Third, based on image entropy, quasi-Newton's method is adopted to obtain the optimal solution for the phase error coefficients. Finally, a new initial estimation method that aims to overcome the local convergence of quasi-Newton's method is proposed. By utilizing the optimal parameters, the well-focused SBISAR image can be achieved. Taking GEO satellite imaging as an example, experiments based on scattering point simulation data verify the effectiveness of the proposed method.**

***Index Terms*—2-D spatial variant phase errors, high-resolution imaging, minimum entropy, satellite on-orbit, space-borne inverse synthetic aperture radar (SBISAR).**

I. Introduction

SPACE orbit resources are further occupied [1] driven by the rapid advancement of space technology and the growing exploration of space resources. One of the objectives of space situation awareness (SSA) is to protect space assets [2] by predicting and assessing space events through the monitoring, tracking, and identifying artificial objects in space, such as active and inactive satellites, orbiting debris, and discarded launcher stages. In addition, satellites in orbit need to be regularly inspected for appearance changes that may cause malfunctions. Hence, SSA plays a crucial role in ensuring the safety and security of satellites located in orbit. High-resolution imaging of objects in space, which serves as the foundation for identifying targets in SSA, has become a significant aspect of space exploration missions. Consequently, all nations engaged in space exploration are actively advancing their capabilities by developing high-resolution optical and radar instruments for the purpose of exploring space [3], [4], [5].

Inverse synthetic aperture radar (ISAR) can provide high-resolution images of moving targets, and has found wide application in radar imaging [6], [7], [8]. Ground-based ISAR is the primary method for radar imaging of orbiting space targets and has made some progress in imaging space targets [9], [10], [11]. However, ground-based ISAR faces limitations due to the visible arc segment of the orbit. High-precision imaging of targets is only possible at specific moments throughout the day. In addition, the Earth's atmosphere causes attenuation of radar signals, especially for high frequency radar. As the target orbital altitude increased, there is a sharp drop in the echo signal-to-noise ratio (SNR). Space-borne ISAR (SBISAR) employs spacecraft and satellites as platforms, enabling strategic orbital maneuvers to position SBISAR in advantageous observation locations for closely monitoring satellite on-orbit. This approach circumvents the challenges associated with atmospheric signal weakening, thus facilitating effective surveillance of observed satellite (OS) on-orbit. Consequently, it is essential to conduct research on imaging techniques for SBISAR.

To identify important features of the OS, the radar image resolution must reach submeter level [2]. This capability proves valuable in accurately classifying and identifying targets for further analysis and application. When the resolution gets higher, it is necessary to consider the ignorable phase errors in conventional ISAR imaging models [12], and this becomes an even more serious problem when imaging OS. About the SBISAR, the OS exhibits slow and intricate relative movements which leads to the coherent processing intervals (CPI) of several hundred seconds when conducting high-resolution imaging. Hence, the

Manuscript received 16 October 2023; revised 28 December 2023; accepted 23 January 2024. Date of publication 29 January 2024; date of current version 13 February 2024. This work was supported by the Reserve Talents Project of National High-Level Personnel of Special Support Program under Grant Y9G0100BF0. *(Corresponding author: Weidong Yu.)*

Yifei Liu and Shenghui Yang are with the Department of Space Microwave Remote Sensing System, Aerospace Information Research Institute, Chinese Academy of Sciences, Beijing 100190, China, and also with the School of Electronic, Electrical and Communication Engineering, University of Chinese Academy of Sciences, Beijing 100039, China (e-mail: liuyifei20@mails.ucas.ac.cn; yangshenghui19@mails.ucas.ac.cn).

Weidong Yu and Shiqiang Li are with the Department of Space Microwave Remote Sensing System, Aerospace Information Research Institute, Chinese Academy of Sciences, Beijing 100190, China (e-mail: yuwd@aircas.ac.cn; lisq@aircas.ac.cn).

Digital Object Identifier 10.1109/JSTARS.2024.3359264

nonnegligible higher order phase errors in the OS imaging model must be accurately characterized. In addition, when imaging the OS, the relative motion between the OS and SBISAR is complex and nonuniform. It will cause a continuous change in the direction and the modulus value of the effective rotation vector, which will lead to continuous change of the image projection plane. As a result, the phase errors exhibit the 2-D spatial-variant characteristic [13]. If the 2-D spatial-variant phase errors are not corrected properly, the final image may get blurred when the range Doppler (RD) algorithm is applied.

The ISAR imaging algorithms for complex maneuvering targets have attracted significant attention [14], [15], [16]. Some imaging methods, such as range instantaneous Doppler (RID) algorithms [17], [18], [19], [20] and autofocus algorithms [16], [21], [22], are presented to achieve the ISAR imaging of maneuvering targets with complex motions. In general, RID algorithms are usually divided into two categories: parametric methods and nonparametric methods. Parametric methods, such as [17], [20], model the echo within a range bin as a linear frequency modulated (LFM) signal or cubic phase signal, implementing ISAR imaging of complex maneuvering targets by estimating the parameters of the signal within each range bin and compensating for the phase error. However, parametric methods treat each range bin as an individual part, ignoring the integrity of the target rotational motion, which reduces the accuracy of parameter estimation and increases the computational complexity. Nonparametric methods which include short-time Fourier transform [23], continuous wavelet transform [24], Wigner–Ville distribution [25], and fractional Fourier transform [26], use time–frequency distribution analysis-based approaches to achieve ISAR imaging. Unfortunately, nonparametric methods encounter challenges in accurately estimating small kinematic parameters due to the relatively slow movement of the OS in comparison to SBISAR. Wang et al. [21] proposed a noise-robust spatial variant phase errors compensation method for aerial maneuvering target ISAR imaging. However, when imaging OS, the CPI is so long that the SBISAR line-of-sight (LOS) cannot be considered constant, which means the high-order coefficients of spatial-variant phase errors cannot be ignored. In [22], a new framework for ISAR imaging of ships that can compensate 2-D high-order spatial variant phase errors is proposed. But the accuracy of approximating high-order coefficients by using second-order coefficient is difficult to meet the high-resolution imaging requirements of SBISAR.

In this article, considering the integrity of the OS motion, an effective algorithm is proposed to compensate the 2-D spatial variant phase errors to obtain a high-resolution image of the OS by SBISAR. First, to reasonably determine the optimal imaging time period for OS, the geometric observation model is established based on the relative on-orbit motion state of SBISAR and OS, and deduces the echo signal model for OS. Second, based on the established echo model, a parametric model of spatial variant phase errors is developed by analyzing the nonuniform rotation of OS with respect to SBISAR carefully. Third, a minimum entropy optimization method based on limited-memory Broyden–Fletcher–Goldfarb–Shanno (L-BFGS) [27] is proposed that aims to search the global optimal parameters of spatial variant phase errors. Besides, combining the relative motions of OS and SBISAR, a new initial value method is applied to improve the convergence efficiency. Finally, by using the optimal parameters to compensate spatial variant phase errors, the well-focused SBISAR images are obtained. The proposed method has the following advantages and innovations. The geometry and echo signal model for SBISAR imaging, based on the complex and nonuniform relative motion of OS on-orbit and SBISAR, are established. Using the orbital parameters of OS and SBISAR, deducing the specific form of the 2-D spatial variant phase errors and combining L-BFGS and image entropy (IE) to search the optimal parameters. The new initial value estimation method is used to accelerate the global convergence speed, thereby achieving high-resolution imaging of SBISAR.

The rest of this article is organized as follows. In Section II, the imaging geometry is established by considering the relative motion states of SBISAR and OS. Furthermore, the signal model is investigated. In Section III, the improved algorithm based on the parametric minimum entropy and the initial value estimation for the OS imaging is proposed to perform 2-D spatial variant phase error compensation. In Section IV, imaging results based on the simulated data and corresponding analysis are given. Finally, Section V concludes this article.

II. Imaging Geometry and Signal Model

According to [28], many satellite are clustered at altitudes from 500 to 1200 km and geosynchronous orbit (GEO) satellites around 36 000 km. This implies that the ISAR image of OS can be obtained by SBISAR with a range of 100 km. Furthermore, as a consequence of the significantly high altitude of GEO satellites, even a slight deviation of 1° in relative orbital inclination will have a significant impact on the slant range and radar LOS between SBISAR and GEO satellite. Therefore, taking into consideration the need for GEO satellite imaging, we will assume as follows in the SBISAR to the OS imaging scenario.

1) The orbit altitude difference between SBISAR and the OS is less than 100 km, with a typical value of 50 km.
2) The difference in inclination between the orbits of the SBISAR and the OS is less than 1°. Usually, the beam of SBISAR is directed upward to track and image the OS, while the remaining orbital parameters align with those of the OS.

For ISAR imaging, the motion of the target relative to the radar can be decomposed into two components: translational and rotational. The radar imaging coordinate system is chosen as the Earth center inertial (ECI) coordinate system, shown in Fig. 1(a). The radar imaging coordinate system with O_s being the origin, where O_s is the geocentric, and the X, Y, Z axes follow the definition of the ECI. R_0 denotes the initial slant range between SBISAR and the OS. The satellite is placed in a Cartesian coordinate (X, Y, Z), called satellite body coordinate system, with the OS rotation center and imaging reference center O as the coordinate origin. Fig. 1(b) shows the OS body coordinates system, and the LOS is defined by the elevation angle. θ_r, θ_p, θ_y represent the pitch, roll, and yaw motions rotating about X,

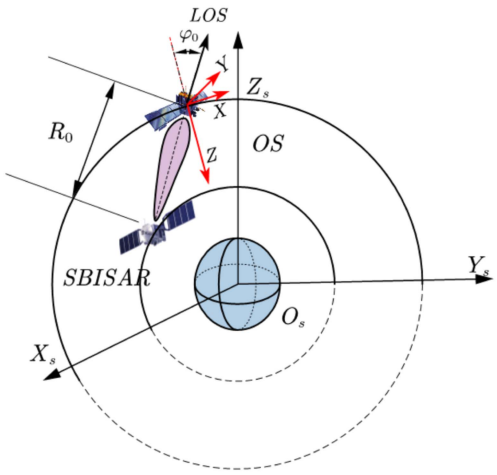

(a)

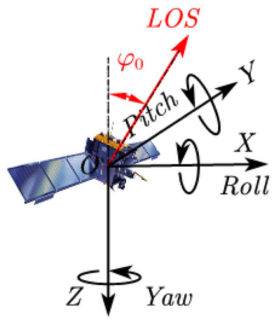

(b)

Fig. 1. Imaging coordinate of the OS. (a) Radar imaging coordinate system. (b) OS body coordinate.

Y, and Z. At the initial moment of imaging, SBISAR observes the satellite at the elevation angle φ_0.

In Section II-A, the radar system parameters are given. Subsequently, the model of echo signal and 2-D spatial variant phase error are introduced in the Section II-B.

A. System Parameters of SBISAR

Assuming that SBISAR beams can continuously track the satellite within the beam scanning range. The azimuth resolution of ISAR can be expressed as

$$\rho_a = \frac{\lambda}{2\Delta\theta} \tag{1}$$

where λ is the wavelength of the signal, and $\Delta\theta$ is the total integration angle. When monitoring the in-orbit status of the OS, it is necessary to accurately describe the appearance details of the OS. To obtain a high-resolution image, the SBISAR system resolution is 5 cm and bandwidth of the SBISAR transmit signal is 3 GHz. It is difficult for low-frequency radar to transmit large-bandwidth signals, and according to (1), the smaller the wavelength of the transmitted signal, the smaller the integration angle required to achieve azimuth resolution. After comprehensive consideration, the SBISAR system exploits the Ka-band signal around 35 GHz as the carrier frequency and the integration angle is calculated to be 6^{circ}. This is significant as it reduces both the runtime of SBISAR system and the amount of echo data. Moreover, employing this band can achieve higher gain with the same antenna size.

TABLE I
PARAMETERS OF THE SBISAR AND OS

Parameter	Value
Carrier frequency	35 GHz
Signal bandwidth	3000 MHz
Range sampling rate	3600 MHz
PRF	50 Hz
Antenna size	0.8*0.8 m
Resolution	0.05 m
Beam scanning range	$\pm 15°$
Average transmit power	200 W
System noise temperature	300 K
Noise figure	5 dB
SBISAR semi-major axis	42116.3 km
SBISAR eccentricity	0
SBISAR inclination	0.11°
SBISAR right ascension of ascending node (RAAN)	89.782°
SBISAR argument of perigee	0°
SBISAR true anomaly	237.557°
OS semimajor axis	42166.3 km
OS inclination	0.105°
OS RAAN	85.179°
OS true anomaly	0°

After simulation, within the CPI, the maximum translation distance of the OS relative to the SBISAR will not exceed 300 m. In the imaging simulation, by setting the azimuth scene width to 500 m, the imaging scene can be completely covered. To receive the echo signal of interested swath, the PRF should satisfy the following equation [29]:

$$\text{PRF} > \frac{D_a}{T_{\text{CPI}} \cdot \rho_a} \tag{2}$$

where ρ_a is azimuth resolution and D_a is azimuth scene width. After calculating, the PRF needs to larger than 10.4 Hz. Thus, the PRF is set to 50 Hz. Based on the above-mentioned basic resolution requirements, the system parameters of SBISAR are given in Table I. The antenna size is 0.8 m $\times$ 0.8 m, so that the beamwidth of the antenna will be about 0.7^{circ}. When imaging OS, in order to achieve a range of 100 km, the average transmit power of SBISAR needs to be considered. The free space radar equation is given by

$$\text{SNR} = \frac{P_t G^2 \lambda^2 \sigma}{(4\pi)^3 R^4} \frac{1}{kT_s B_i N_f} \tag{3}$$

The SNR for detection which may be taken as 15 dB; k is Boltzmann's constant; σ is the radar cross section for the OS, which can be assumed as 2 m^2; other parameters are given in Table I. The antenna gain can be calculated form antenna size. After considering the 2-D pulse compression gain, the radar detection range can be larger without losing SNR.

B. Echo Signal Model of SBISAR

Assuming that the SBISAR transmits an LFM signal, the echoes of an arbitrary scatterer P on the OS can be written

as

$$s_p(t_r;t_m)=\sigma_p\,\mathrm{rect}\left(\frac{t_r-\frac{2R_p(t_m)}{c}}{T_p}\right)\cdot\exp\left[j2\pi f_c\left(t-\frac{2R_p(t_m)}{c}\right)\right]\cdot\exp\left[j\pi\gamma\left(t_r-\frac{2R_p(t_m)}{c}\right)^2\right] \tag{4}$$

where

$$\mathrm{rect}(u)=\begin{cases}1 & |u|\le\frac{1}{2}\\ 0 & |u|>\frac{1}{2}\end{cases}$$

where σ_p, T_p, c, f_c, and γ denote the reflection coefficient, pulse width, speed of light, carrier frequency, and chirp rate, respectively. $t=t_m+t_r$ denotes the full time, where t_r is the fast time and t_m is the slow time. The coordinate of P can be denoted as (x_p,y_p,z_p) in the OS's body coordinate. $R_p(t_m)$ is the distance between the SBISAR and the scatterer P at the time t_m. After demodulation, range compression, and applying the Fourier transform with respect to t_r in (4), one obtains

$$S_p(f_r;t_m)=\sigma_p\exp\left[-j2\pi\frac{2R_p(t_m)}{c}(f_r+f_c)\right]. \tag{5}$$

Similar to traditional ISAR imaging, the instantaneous slant range $R_p(t_m)$ in the case of SBISAR imaging of OS can be divided as two parts: translational motion part $R_t(t_m)$ and rotational motion part $R_{\mathrm{rot}}(t_m)$, which can be expressed by

$$R_p(t_m)=R_t(t_m)+R_{\mathrm{rot}}(t_m). \tag{6}$$

According to [30], $R_{\mathrm{rot}}(t_m)$ can be expressed by the OS's rotation matrix $\mathbf{M}_{\mathrm{rot}}(t_m)$ as

$$R_{\mathrm{rot}}(t_m)=\left[\mathbf{M}_{\mathrm{rot}}(t_m)\cdot\mathbf{P}\right]^T\cdot\mathbf{i}_{\mathrm{los}} \tag{7}$$

where $\mathbf{P}$ is the position vector of point P in the coordinate of OS body. Different from conventional ISAR imaging, the unit vector $\mathbf{i}_{\mathrm{los}}$ of radar LOS is time varying during long CPI. In order to provide a more precise description of the maneuvering characteristics of the OS, the unit vector of LOS is modeled as the function of slow time, expressed by

$$\mathbf{i}_{\mathrm{los}}=\left[-\sin(\varphi(t_m)),0,-\cos(\varphi(t_m))\right]^T. \tag{8}$$

The OS rotates on the pitch axis during inertial motion in orbit, so $\mathbf{M}_{\mathrm{rot}}(t_m)$ can be expressed as t_m [31]

$$\mathbf{M}_{\mathrm{rot}}(t_m)=\begin{bmatrix}\cos[\theta_p(t_m)] & 0 & \sin[\theta_p(t_m)]\\ 0 & 1 & 0\\ -\sin[\theta_p(t_m)] & 0 & \cos[\theta_p(t_m)]\end{bmatrix} \tag{9}$$

where $\varphi(t_m)$ and $\theta_p(t_m)$ can be expressed by (10). The detailed analysis of $\varphi(t_m)$ and $\theta_p(t_m)$ is provided in Appendix A

$$\begin{cases}\varphi(t_m)=\varphi_0+\omega_\varphi t_m+\frac{\dot\omega_\varphi}{2}t_m^2\\ \theta_p(t_m)=\omega_p t_m.\end{cases} \tag{10}$$

Based on the second-order Taylor polynomial approximation $\cos(\theta)\approx1-\frac{1}{2}\theta^2$ and $\sin(\theta)\approx\theta$, substituting (8)–(9) into (7). $R_{\mathrm{rot}}(t_m)$ can be modeled as a high-order coefficient of t_m

$$R_{\mathrm{rot}}(t_m)=K_0+K_1t_m+K_2t_m^2+K_3t_m^3+K_4t_m^4+K_5t_m^5+K_6t_m^6 \tag{11}$$

where the detailed expressions of coefficients are given in Appendix B. Substituting (11) and (6) into (5), given by

$$S_p(f_r;t_m)=\sigma_p\cdot\exp\left[-j\frac{4\pi R_t(t_m)}{c}(f_r+f_c)\right]\cdot\exp\left[-j\frac{4\pi f_r}{c}K_0\right]\cdot\exp\left[-j\Delta\Phi_R\right]\cdot\exp\left[-j\frac{4\pi f_c}{c}(K_0+K_1t_m)\right]\cdot\exp\left[-j\Delta\Phi_A\right] \tag{12}$$

where $\exp[-j\Delta\Phi_R]$ represents the terms of migration through range cell (MTRC) and can be divided into six parts: $\exp[-j\Delta\Phi_{R,1}]$— $\exp[-j\Delta\Phi_{R,6}]$, $\exp[-j\Delta\Phi_A]$ represents the terms of spatial variant phase errors and can be divided into five parts: $\exp[-j\Delta\Phi_{A,2}]$— $\exp[-j\Delta\Phi_{A,6}]$. To determine the order of $R_{\mathrm{rot}}(t_m)$ in the SBISAR echo signal model, we will analyze which items in $\exp[-j\Delta\Phi_R]$ and $\exp[-j\Delta\Phi_A]$ cannot be ignored.

$\Delta\Phi_{R,1}=4\pi f_rK_1t_m/c$, $\Delta\Phi_{R,2}=4\pi f_rK_2t_m^2/c$, $\Delta\Phi_{R,3}=4\pi f_rK_3t_m^3/c$, $\Delta\Phi_{R,4}=4\pi f_rK_4t_m^4/c$, $\Delta\Phi_{R,5}=4\pi f_rK_5t_m^5/c$, and $\Delta\Phi_{R,6}=4\pi f_rK_6t_m^6/c$ represent the first-, second-, third-, fourth-, fifth-, and sixth-order MTRCs, respectively. $\Delta\Phi_{A,2}=4\pi f_cK_2t_m^2/c$, $\Delta\Phi_{A,3}=4\pi f_cK_3t_m^3/c$, $\Delta\Phi_{A,4}=4\pi f_cK_4t_m^4/c$, $\Delta\Phi_{A,5}=4\pi f_cK_5t_m^5/c$ and $\Delta\Phi_{A,6}=4\pi f_cK_6t_m^6/c$ represent the second-, third-, fourth-, fifth-, and sixth-order spatial variant phase errors. According to [32], if $\Delta\Phi_A<\pi/4$, the influence of corresponding terms on spatial variant phase errors can be negligible. Similarly, if $\Delta\Phi_R<\pi/4$, the corresponding terms can be negligible.

Subsequently, simulation experiments are conducted to analyze which terms can be disregarded in the SBISAR imaging of GEO satellites. Assuming the size of satellite is 3 m × 3 m × 10 m, we set a scatterer point $P(2,2,6)$ farthest from the geometric center of the OS to illustrate the issue. The simulation parameters are shown in Table I, and the relative motion parameters can be calculated as follows: ω_p is 7.291×10^{-5} rad/s, ω_φ is 1.0965×10^{-5} rad/s, and $\dot\omega_\varphi$ is -1.2562×10^{-5} rad/s^2.

Denoting the $\exp[-j\Delta\Phi_{R,1}]$—$\exp[-j\Delta\Phi_{R,6}]$ as MTRC1-6, $\exp[-j\Delta\Phi_{A,2}]$—$\exp[-j\Delta\Phi_{A,6}]$ as APE2-6. Their values are shown in Table II. From Table II, since MTRC1, MTRC2, APE2, and APE3 are all greater than $\pi/4$, it is necessary to compensate those terms in imaging process. Therefore, $R_{\mathrm{rot}}(t_m)$ can be rewritten as

$$R_{\mathrm{rot}}(t_m)=K_0+K_1t_m+K_2t_m^2+K_3t_m^3. \tag{13}$$

In addition, the terms of MTRC must be conserved to second order in echo signal.

By analyzing the form of the coefficients in (13), K_2 and K_3 are linear with respect to K_0 and K_1

$$K_2=\zeta_zK_0+\zeta_xK_1$$

TABLE II
VALUES OF MTRC AND AZIMUTH PHASE ERROR

	Real values	Ideal values
MTRC1	7.95	$> \pi/4$
MTRC2	1.19	$> \pi/4$
MTRC3	0.06	$< \pi/4$
MTRC4	7.68×10^{-3}	$< \pi/4$
MTRC5	8.47×10^{-5}	$< \pi/4$
MTRC6	2.37×10^{-7}	$< \pi/4$
APE2	23.24	$> \pi/4$
APE3	1.18	$> \pi/4$
APE4	0.15	$< \pi/4$
APE5	1.65×10^{-3}	$< \pi/4$
APE6	4.62×10^{-6}	$< \pi/4$

$$K_3 = \xi_z K_0 + \xi_x K_1 \tag{14}$$

where the detailed deduction of this technique is given in the Appendix A. Substituting (14) and (11) into (6), the instantaneous slant range between SBISAR and scatterer P on the OS can be re-expressed as

$$\begin{aligned} R_p(t_m) &= R_t(t_m) + R_{\text{rot}}(t_m) \\ &\approx R_t(t_m) + K_0 + K_1 t_m \\ &\quad + (\zeta_z K_0 + \zeta_x K_1) t_m^2 + (\xi_z K_0 + \xi_x K_1) t_m^3. \end{aligned} \tag{15}$$

Finally, the received echo signal of the OS with complex rotational motion in the SBISAR can be rewritten as

$$\begin{aligned} &S_p(f_r; t_m) \\ &\approx \sigma_p \cdot \exp\left[-j\frac{4\pi R_t(t_m)}{c}(f_r + f_c)\right] \\ &\cdot \exp\left[-j4\pi\frac{K_0 + K_1 t_m + (\zeta_z K_0 + \zeta_x K_1) t_m^2}{c}(f_r + f_c)\right] \\ &\cdot \exp\left[-j4\pi\frac{(\xi_z K_0 + \xi_x K_1) t_m^3}{c}(f_r + f_c)\right]. \end{aligned} \tag{16}$$

C. 2-D Spatial Variant Phase Errors for the OS With Complex Motion

To examine the phase error term, which has an impact on the imaging process, and considering the phase error analysis in Appendix B, a possible approach is to reframe the (16) as

$$\begin{aligned} &S_p(f_r; t_m) \\ &\approx \sigma_p \cdot \exp\left[-j\frac{4\pi}{c}K_0 f_r\right] \cdot \exp\left[-j\frac{4\pi}{c}f_c K_1 t_m\right] \\ &\cdot \exp\left[-j4\pi\frac{K_0}{c}f_c\right] \cdot \exp\left[-j\frac{4\pi R_t(t_m)}{c}(f_r + f_c)\right] \\ &\cdot \exp\left[-j4\pi\frac{(\zeta_z K_0 + \zeta_x K_1) t_m^2 + (\xi_z K_0 + \xi_x K_1) t_m^3}{c} f_c\right] \\ &\cdot \exp\left[-j4\pi\frac{K_1 t_m + K_2 t_m^2}{c} f_r\right]. \end{aligned} \tag{17}$$

Noticed that the phase in (17) can be considered as six parts. The first term corresponds to the scatterer's range position after range compression, the second term is the linear phase term corresponds to the Doppler, the third term is a constant term that has no contribution to imaging, the fourth term is the phase errors of translational motion, the fifth term represent the 2-D spatial variant phase errors, the last one corresponds to the MTRC caused by the OS's complex rotational motion. A well-focused SBISAR image can only be achieved by accurately compensating the fourth through sixth terms. In general, some standard translational motion compensation (TMC) algorithms in ISAR imaging can effectively compensate the translational motion [33], [34], [35]. The MTRC can also be compensated by some standard methods, such as keystone transform (KT) [36] and generalized KT [37]. For each scatterer, the sixth term corresponds to the completely different phase error, which certainly exacerbates the difficulty of compensation. For this reason, we focus on the 2-D spatial variant phase.

After TMC and MTRC correction, echo signal can be expressed as

$$\begin{aligned} &S_p(f_r; t_m) \\ &= \tilde{S}_p(f_r; t_m) \cdot \exp\left[-j\frac{4\pi}{c}f_c(\zeta_z K_0 + \zeta_x K_1) t_m^2\right] \\ &\cdot \exp\left[-j\frac{4\pi}{c}f_c(\xi_z K_0 + \xi_x K_1) t_m^3\right] \end{aligned} \tag{18}$$

where $\tilde{S}_p(f_r; t_m)$ is the signal that is not polluted by 2-D spatial variant phase errors, given by

$$\begin{aligned} &\tilde{S}_p(f_r; t_m) \\ &= \sigma_p \cdot \exp\left[-j\frac{4\pi}{c}K_1 f_c t_m\right] \cdot \exp\left[-j\frac{4\pi}{c}K_0 f_r\right]. \end{aligned} \tag{19}$$

Applying the inverse discrete Fourier transform (IDFT) to (18) with respect to f_r, given by

$$\begin{aligned} &s_p(m, n) \\ &= \tilde{s}_p(m, n) \cdot \exp\left[-j\frac{4\pi}{c}f_c(\zeta_z K_0 + \zeta_x K_1) n^2\right] \\ &\cdot \exp\left[-j\frac{4\pi}{c}f_c(\xi_z K_0 + \xi_x K_1) n^3\right] \end{aligned} \tag{20}$$

where $m = 1, 2, \ldots, M$ represents the range indices and M is the number of range cells, and $n = 1, 2, \ldots, N$ represents the azimuth indexes in synthetic aperture time and N is the total number of azimuth aperture. Respectively, $s_p(m, n)$ and $\tilde{s}_p(m, n)$ denote the discrete form of $s_p(t_r, t_m)$ and $\tilde{s}_p(t_r, t_m)$.

If the coefficients $(\zeta_x, \zeta_z, \xi_x, \xi_z)$ of the spatial variant phase errors are precisely known, the well-focused SBISAR image $g(m, k)$ can be obtained by applying IDFT along the cross-range direction after multiplying the 2-D spatial variant phase errors compensation term into (20), given by

$$g(m, k) = \frac{1}{N}\sum_{n=0}^{N-1} \exp\left[j2\pi\frac{kn}{N}\right] \cdot s_p(m, n)$$

$$\cdot \exp\left[j\frac{4\pi}{c}f_c\left(\zeta_z K_0+\zeta_x K_1\right)n^2\right]$$
$$\cdot \exp\left[j\frac{4\pi}{c}f_c\left(\xi_z K_0+\xi_x K_1\right)n^3\right]. \quad (21)$$

Based on the deduction in Appendix B, (21) is re-expressed as

$$g(m,k)=\frac{1}{N}\sum_{n=0}^{N-1}\exp\left[j2\pi\frac{kn}{N}\right]\cdot s_p(m,n)$$
$$\cdot \exp\left[-j\left(C_x m+C_z k\right)n^2\right]$$
$$\cdot \exp\left[-j\left(Q_x m+Q_z k\right)n^3\right] \quad (22)$$

where $C_x=-2\pi\zeta_x/T_a, C_z=-2\pi\zeta_z c/\lambda B, Q_x=-2\pi\xi_x/T_a$, and $Q_z=-2\pi\xi_z c/\lambda B$. The subscripts "$x$" and "$z$" of the spatial variant phase errors coefficients represent the errors components at different coordinates of the scatterers.

Notice that, the 2-D spatial variant phase errors are determined by four unknown parameters, and the well-focused SBISAR image can be achieved by precisely compensating the 2-D spatial variant phase errors terms $\exp[j(C_x m+C_z k)n^2]$ and $\exp[j(Q_x m+Q_z k)n^3]$. Obviously, compensating the phase error poses a significant challenge due to its spatially variant properties for different values of m and k. Therefore, the following key task is to find the optimum values of (C_x, C_z, Q_x, Q_z).

III. Proposed Processing Algorithm

For solving these problems, an effective parameter estimation algorithm is established to obtain well-focused SBISAR image of the OS, and a new initial value estimation approach is proposed based on the geometric relationship between SBISAR and the OS.

A. Parameters Estimation Method by Parametric Minimum Entropy

For describing the problem clearly, we define the vector of parameters to be estimated as $\Re=(\tilde{C}_x,\tilde{C}_z,\tilde{Q}_x,\tilde{Q}_z)$ and rewritten the complex image after phase correction as

$$\tilde{g}(m,k;\Re)=\frac{1}{N}\sum_{n=0}^{N-1}\exp\left[j2\pi\frac{kn}{N}\right]\cdot s_p(m,n)$$
$$\cdot \exp\left[-j\left(\tilde{C}_x m+\tilde{C}_z k\right)n^2\right]$$
$$\cdot \exp\left[-j\left(\tilde{Q}_x m+\tilde{Q}_z k\right)n^3\right] \quad (23)$$

if the vector $\Re$ could be estimated accurately, the well-focused image can be obtained by (23).

The problem of estimating the parameters in the ISAR imaging can be considered as an unconstrained optimization problem for the objective function variables. In current parameter estimation methods utilizing optimization techniques, the global image quality indicators for ISAR images, such as entropy [38], contrast, and sharpness, are usually chosen as the objective function. It can also reflect the execution of the parameter estimation process. The entropy reflects the degree of chaos of the ISAR image, and as the entropy decreases, the quality of the ISAR image improves. Therefore, IE is adopted as the objective function in the unconstrained optimization problem to estimate the spatial variant phase errors. The IE of the OS can be define as a function of $\Re$, given by

$$E_g(\Re)=\ln(S_g)-\frac{1}{S_g}\sum_{m=0}^{M}\sum_{k=0}^{N}|\tilde{g}(m,k;\Re)|^2$$
$$\cdot \ln|\tilde{g}(m,k;\Re)|^2 \quad (24)$$

where S_g is the image intensity, given by

$$S_g=\sum_{m=0}^{M}\sum_{k=0}^{N}|\tilde{g}(m,k;\Re)|^2. \quad (25)$$

The optimal estimated vector $\hat{\Re}=(\hat{C}_x,\hat{C}_z,\hat{Q}_x,\hat{Q}_z)$ can be obtained by minimizing the objective function $E_g(\Re)$, expressed as follows:

$$\hat{\Re}=\arg\min_{\Re} E_g(\Re). \quad (26)$$

In general, there are many standard algorithms that can solve this problem, such as particle swarm optimization [39], ant colony optimization [40], and genetic algorithm. However, when estimating multiple parameters, these algorithms require a lot of processing time. In this work, we employs the Newton method based on L-BFGS to enhance computational efficiency for parameter estimation of IE. The gradient matrix of the IE $\mathbf{Y}=[\frac{\partial E_g(\Re)}{\partial C_x},\frac{\partial E_g(\Re)}{\partial C_z},\frac{\partial E_g(\Re)}{\partial Q_x},\frac{\partial E_g(\Re)}{\partial Q_z}]^T$ needs to be computed, and the partial derivative of C_x can be obtained by follows:

$$\frac{\partial E_g(\Re)}{\partial C_x}=-\frac{1}{S_g}\sum_{m=0}^{M}\sum_{k=0}^{N}\left[1+\ln|\tilde{g}(m,k;\Re)|^2\right]$$
$$\times\frac{\partial \ln|\tilde{g}(m,k;\Re)|^2|}{\partial C_x} \quad (27)$$

where $|\tilde{g}(m,k;\Re)|^2=\tilde{g}(m,k;\Re)\cdot\tilde{g}^*(m,k;\Re)$, and

$$\frac{\partial|\tilde{g}(m,k;\Re)|^2}{\partial C_x}=\tilde{g}^*(m,k;\Re)\cdot\frac{\partial\tilde{g}(m,k;\Re)}{\partial C_x}$$
$$+\tilde{g}(m,k;\Re)\cdot\frac{\partial\tilde{g}^*(m,k;\Re)}{\partial C_x}$$
$$=2\,\mathrm{Re}\left[\tilde{g}^*(m,k;\Re)\cdot\frac{\partial\tilde{g}(m,k;\Re)}{\partial C_x}\right]. \quad (28)$$

Based on (23), we have

$$\frac{\partial\tilde{g}(m,k;\Re)}{\partial C_x}=\frac{1}{N}\sum_{n=0}^{N-1}\exp\left[j2\pi\frac{kn}{N}\right]\cdot s_p(m,n)$$
$$\cdot \exp\left[-j\left(C_x m+C_z k\right)n^2\right]$$
$$\cdot \exp\left[-j\left(Q_x m+Q_z k\right)n^3\right]\cdot\left(-jmn^2\right). \quad (29)$$

The remaining partial derivatives are similar to those derived for C_x, and the detailed form is given in Appendix C. In the L-BFGS algorithm, the gradient matrix of the objective function is employed to provide an approximation of the Hessian matrix.

This approximation serves to effectively decrease the computational complexity. It is common for unconstrained optimization algorithms to necessitate parameter iteration to identify the optimal values. Consequently, a crucial method for enhancing computational efficiency involves parameter initialization, where initial values in proximity to the optimal solution are selected to expedite the iteration process. In Section III-B, an initial estimation of motion parameters for the OS by SBISAR is proposed.

The iterative flow of the L-BFGS algorithm is as follows. Define the 2-D spatial variant phase errors obtained through the initial value estimation method in Section III-B as $\Re = (\tilde{C_{x0}}, \tilde{C_{z0}}, \tilde{Q_{x0}}, \tilde{Q_{z0}})$. The update equation for the descent direction $\mathbf{d}_{\mathrm{i}}$ for the ith iteration is

$$\mathbf{d}_{\mathrm{i}} = -\mathbf{H}_i \nabla E\left(\Re_{\mathrm{i}}\right) \tag{30}$$

where $\mathbf{H}_i$ is the Hessian matrix of IE in the ith iteration and $\Re_{\mathrm{i}}$ is the vector of parameters in the ith iteration. In the $(i+1)$th iteration, the $\Re_{\mathrm{i}}$ can be expressed as

$$\Re_{i+1} = \Re_i + \alpha_i \mathbf{d}_i \tag{31}$$

where α_i is the descent step in the ith iteration that satisfies the Wolfe criterion, and the update equation of Hessian matrix are given by

$$\begin{cases} \mathbf{H_{i+1}} = \left(\mathbf{V}_i\right)^T \mathbf{H}_i \mathbf{V}_i + \boldsymbol{\rho}_i \mathbf{s}_i \left(\mathbf{s}_i\right)^T \\ \boldsymbol{\rho}_i = \frac{1}{\left(\mathbf{y}_i\right)^T \mathbf{s}_i'}, \mathbf{V}_i = I - \boldsymbol{\rho}_i \mathbf{y}_i \left(\mathbf{s}_i\right)^T \end{cases} \tag{32}$$

where $\mathbf{s}_i = \Re_{i+1} - \Re_i$ and $\mathbf{y}_i = \nabla E(\Re_{\mathrm{i}+1}) - \nabla E(\Re_{\mathrm{i}})$, respectively.

B. Initialized Estimation of Motion Parameters

The problem of correcting phase errors in SBISAR imaging of the OS, specifically the 2-D spatial variable phase error, is formulated as a global optimization problem without constraints. To solve this problem, the L-BFGS method is employed. The Newton method exhibits local convergence, indicating that the initial solution must be in close proximity to the optimal solution. In addition, for ill-conditioned problems, the convergence domain of the quasi-Newton algorithm decreases, requiring a more precise selection of initial values. To address this problem, a novel method for estimating initial values is proposed.

As derived earlier, the parameters of 2-D spatial variant phase errors are determined by the motion parameters of the OS. Therefore, it is crucial to acquire an iterative initial value for the spatial variant phase error parameters by estimating the nonuniform rotation of the satellite through the geometric relationship between the OS and SBISAR. As shown in Fig. 2, θ_{Beam}, R, H_r, ΔH, V_t, and V_r denote the beam scanning angle, the slant range between SBISAR and the OS, the orbital altitude of SBISAR, the orbital altitude difference between SBISAR and the OS, the speed of SBISAR and the speed of the OS. The angle to the target called angle-of-arrival, which can be measured by monopulse technology [41]. Thus, θ_{Beam} is measured by the monopulse technology. The center of SBISAR, the OS and geocentric are denoted by A, B, and O. The distance of the OS from the geocentric can be determined using the cosine theorem in Fig. 2,

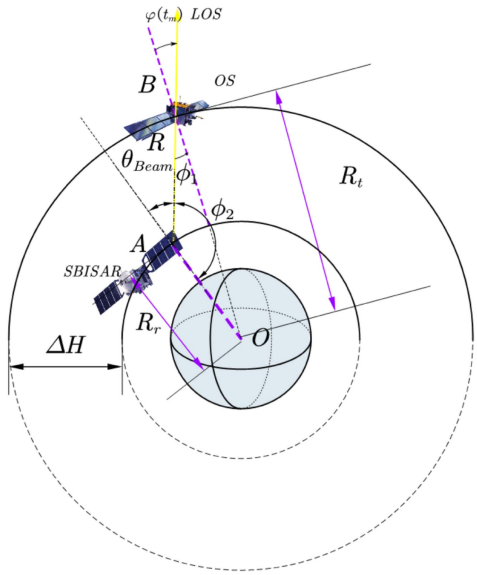

Fig. 2. Relative geometry of SBISAR and the OS.

given by

$$R_t = \sqrt{R_r^2 + (c\tau/2)^2 - 2R_r(c\tau/2)\cos\left(\phi_2\right)} \tag{33}$$

where τ, R_r, and c are the round-trip time delay, the range form SBISAR and geocentric and light speed. $\phi_2 = \pi - \theta_{\mathrm{Beam}}$, and the GEO target's pitch axis rotation speed is its own orbital angular velocity

$$\omega_{\mathrm{pitch}} = \sqrt{\frac{R_t^3}{GM_\oplus}} \tag{34}$$

where $GM_\oplus = 398600.4405(\mathrm{km}^3 \cdot \mathrm{s}^{-2})$ is gravitational coefficient. Upon obtaining the value of R_t, one can then apply the sine theorem to determine ϕ_1, denoting the $\varphi(t_m)$ in the coordinate system of the target body located in GEO

$$\frac{R_r}{\sin\left(\phi_1\right)} = \frac{R_t}{\sin\left(\phi_2\right)}. \tag{35}$$

After obtaining $\varphi(t_m)$, the ω_φ and $\dot{\omega}_\varphi$ can be achieved by

$$\begin{cases} \omega_\varphi = \frac{d\varphi(t_m)}{dt_m} \\ \dot{\omega}_\varphi = \frac{d^2\varphi(t_m)}{dt_m^2}. \end{cases} \tag{36}$$

Based on (34)–(36), ω_{pitch} and $\mathbf{i}_{\mathrm{los}}$ can be obtained and $\Re = (\tilde{C_x}, \tilde{C_z}, \tilde{Q_x}, \tilde{Q_z})$ can then be estimated as the initial iteration values for the proposed algorithm of Section III-A. For clarity, we present the flowchart of SBISAR correction method for 2-D spatial variant phase errors in Fig. 3. First, the distorted image can be obtained by applying TMC method and KT to echo signal. Second, the proposed initial value estimation method is utilized to obtain iterative initial values $\Re = (\tilde{C_x}, \tilde{C_z}, \tilde{Q_x}, \tilde{Q_z})$, and the distorted image is transformed into the azimuth phase history data domain by DFT. Third, using the iterative initial values and L-BFGS method on the IE to find the optimal values for the terms of 2-D spatial variant phase errors. Finally, the echo data are compensated according to the optimal estimated parameters.

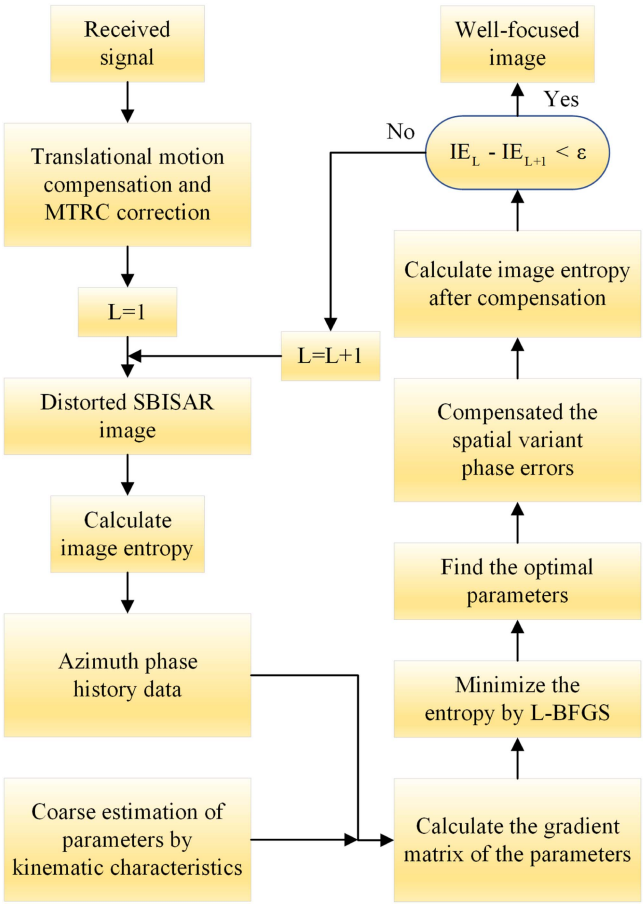

Fig. 3. Flowchart of the proposed SBISAR imaging method.

The iteration concludes when the disparity in IE between two consecutive iterations falls below a specified threshold.

C. Computational Complexity Analysis

Typically, the computational complexity is represented by the number of the floating-point operations (FLOPs). $N \log_2 N$ FLOPs are needed to compute N-point FT or IFT. Multiplying N points of data once requires N FLOPs and calculating the IE of a SBISAR image with size (M, N) requires MN FLOPs. For the proposed imaging procedure, the realization procedure can be divided into four parts. The first and second one is coarse RD imaging and KT, respectively. For the former, the computational complexity is $O_{\text{RD}}(2\,MN \cdot \log_2 M + MN + MN * \log_2 N)$ that is composed of range compression and azimuth compression. For the latter, the sinc interpolation is adopted to realize the calculation, and the computational complexity is $O_{\text{KT}}(M^2 N)$. The third and last one is the minimum entropy optimization and the azimuth compression. The computational complexity mainly lies in the calculation of $\nabla E(\Re)$ and $\mathbf{H}$ for the former. Supposed that the iteration times of L-BFGS is U, and the iterative number of searching α is V. The computational complexity of this part is $O_{\text{MBO}}(U((V+2)MN \cdot 4\log_2 M + MN))$, where $V+2$ denotes that the IE is computed twice before proceeding to search for the α. The computational complexity of the last part is $O_{\text{AO}}(MN \cdot \log_2 N)$. Thus, the total computational complexity

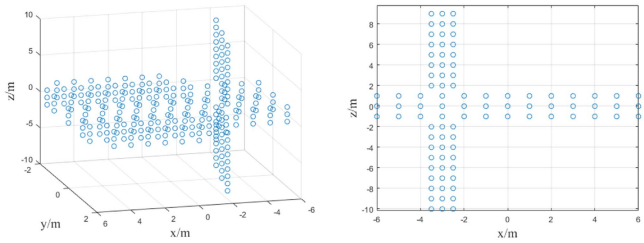

Fig. 4. Satellite model. (a) 3-D satellite model. (b) Top view of the satellite model.

TABLE III
RADAR AND THE OS SIMULATION PARAMETERS

Parameter	Value
CPI	962 s
Rotational velocity of pitch	7.291×10^{-5} rad/s
Initial rotation angle	3.233×10^{-5} rad
Rotational velocity	1.0965×10^{-5} rad/s
Rotational acceleration	-1.2562×10^{-5} rad/s^2

of the SBISAR imaging method is

$$C_{\text{PRO}} = O\left\{\begin{array}{l} 2\,MN \cdot \log_2 M + MN^* \log_2 N \\ +M^2 N + MN + MN \cdot \log_2 N \\ +U\left((V+2)MN \cdot 4\log_2 M + MN\right) \end{array}\right\}. \quad (37)$$

IV. Experimental Results and Performance Analysis

In this section, the performance of the proposed algorithm will be evaluated by using simulated data. For a 3-D rotating OS point scattering model, the phase error compensation is performed by RD, RD-Keystone (RDK), method in [20] and the proposed algorithm, respectively. 2-D high-resolution imaging requires a high sampling rate for SBISAR systems, resulting in excessive echo data within long CPI. Therefore, consider using the varied sampling start method to receive echo signals in the SBISAR system. TMC is divided into two parts: range alignment and phase adjustment. The CPI is divided into multiple subapertures by varied sampling start method, and the range alignment of the echoes within each subapertures is achieved by the cumulative cross-correlation method. Then, the global range alignment is realized based on the MMSE criterion, and more details about the process can be found in [34]. Finally, the phase alignment is achieved by the energy extraction of prominent points. The point can be extracted by applying the Radon transform to the range-aligned echoes or using the minimum variance method. The contrast and entropy of image are used as evaluation metrics for different algorithms and all results demonstrate the availability of the proposed algorithm.

A. Simulation Results

In this section, some imaging results based on simulation data are provided to verify the effectiveness of the proposed method. Fig. 4 illustrates the distribution of the 3-D scattering model of the OS, and the simulation parameters are presented in Table III. The system parameters of SBISAR are given in Table I.

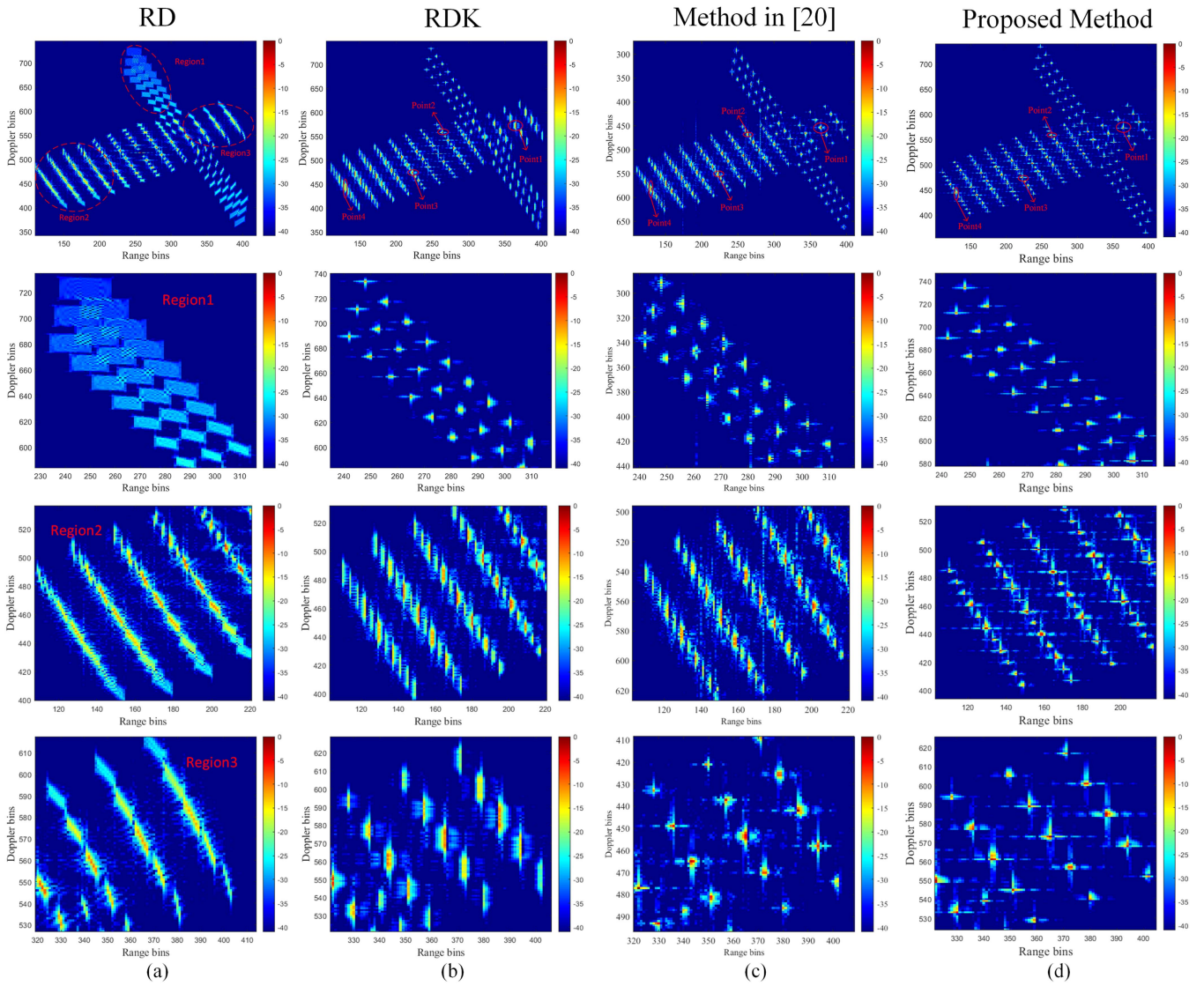

Fig. 5. Experimental results with different imaging methods. (a) Imaging results obtained by RD. (b) Imaging results obtained by RDK. (c) Imaging results obtained by the method in [20]. (d) Imaging results obtained by the proposed method.

The SBISAR imaging results with the RD algorithm, RDK algorithm, method in [20], and our proposed algorithm are provided in Fig. 5, where the first row is the complete result and the rest is the enlarged image. The RD algorithm achieves ISAR imaging by 2-D FFT after TMC, which can only compensate for the nonspatial variant phase errors. Therefore, the image of complex motion OS is still severely distorted in both range and azimuth direction. The RDK compensates the MTRC by using KT after TMC, leaving the image still defocused in the azimuth direction. The method in [20] models the 2-D spatial variant phase errors in each range bin as the high-order polynomial. By utilizing the instantaneous mutual correlation function and scale transformation to estimate the target motion parameters, correcting the 2-D spatial variant phase error for imaging the target. Fig. 6 shows the range bins within the red oval box corresponding to different images obtained by different methods. Combined with Fig. 5(a), since the RD algorithm cannot correct the MTRC of the scatterer, the energy of the scatterer diffuses into adjacent range bins. Even though the scatterer's envelope within each range bin is not broadened, the image is still distorted. After KT and method in [20], the scatterers still have wide main lobe, resulting in blurring of the SBISAR image. However, the width of the main lobe gets smaller and the sidelobes almost disappear by using our proposed method.

Fig. 8 shows the variation of IE with the iteration times of the proposed method. It can be seen that the algorithm in this work needs only five iterations to reach convergence, which proves the high computational efficiency of the method. The IE and image contrast (IC) are considered to quantitatively assess the imaging quality of the SBISAR image. The entropy for a image $g(m,k)$ is given by (24), and the contrast can be defined by

$$\mathrm{IC} = \frac{\sqrt{A\left\{\left[|g(m,k)|^2 - A\left[|g(m,k)|^2\right]\right]^2\right\}}}{A\left[|g(m,k)|^2\right]} \tag{38}$$

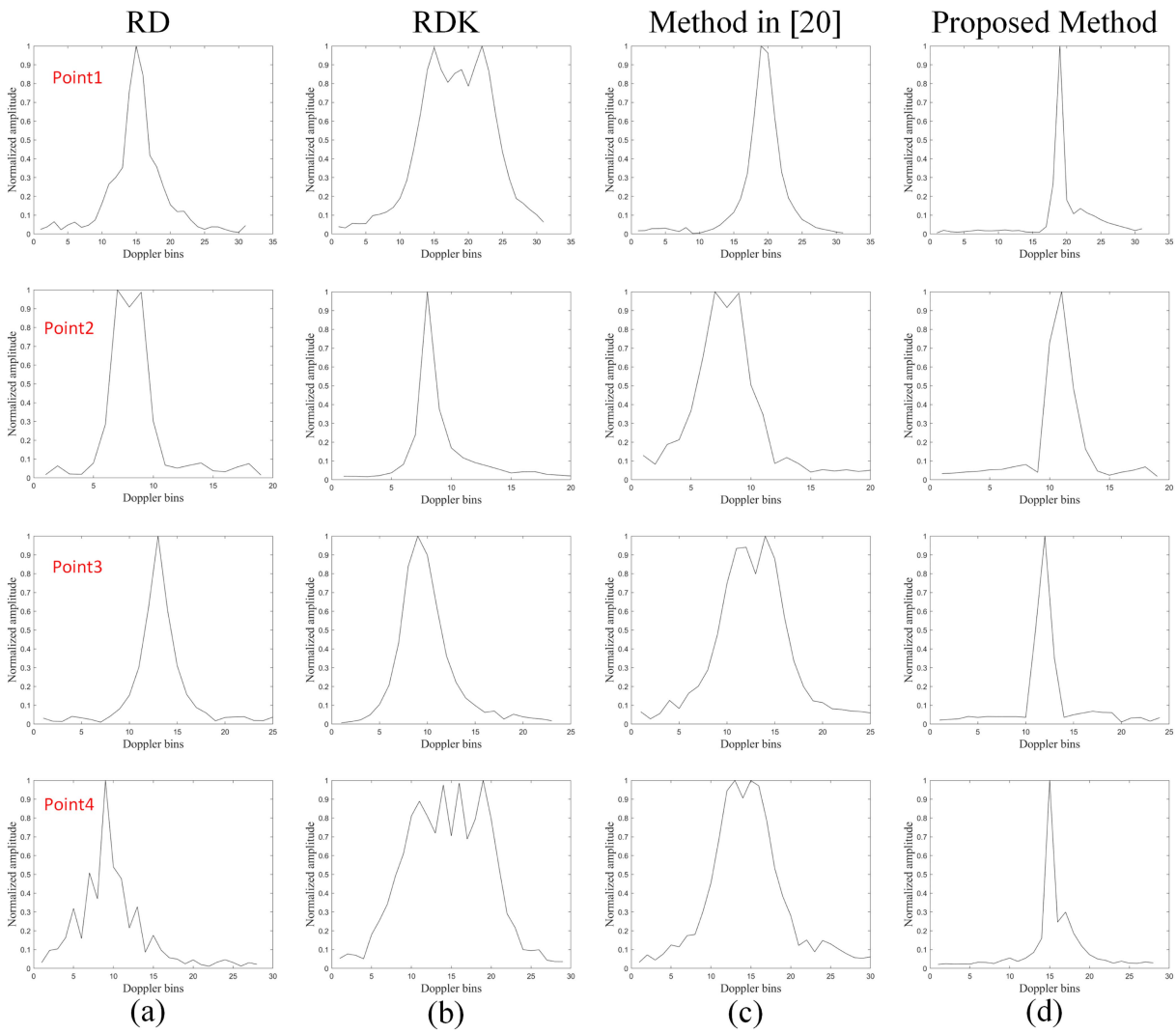

Fig. 6. Images of different range bins. (a) Images of different range bins obtained by RD. (b) Images of different range bins obtained by RDK. (c) Images of different range bins obtained by method in [20]. (d) Images of different range bins obtained by the proposed method.

TABLE IV
ENTROPY AND CONTRAST OF SBISAR IMAGES FOR DIFFERENT METHODS

	RD	RDK	Method in [20]	Proposed method
IC	5.3653	6.1193	6.6260	7.5241
IE	6.4603	6.3316	6.3726	6.0693

where $A[\cdot]$ represents the image spatial mean over the coordinates (m, k). Table IV shows the IE and IC of different methods. The results show that the proposed method in this article has maximum IC and minimum IE with the best image focusing quality, indicating the proposed method may be more suitable for high-resolution SBISAR imaging.

B. Performance Under Different SNRs

In this section, to construct the noisy environment, we introduce Gaussian white noise to the received signal. Subsequently, the effectiveness of various methods including RD, RDK, method in [20], and the proposed method will be discussed. The SNR is defined as

$$\mathrm{SNR} = 10\log_{10}\left[\frac{P_{\mathrm{signal}}}{P_{\mathrm{noise}}}\right] \tag{39}$$

where P_{signal} is the mean power of the signal and P_{noise} is the power of the noise.

Fig. 7 provides the imaging results of different methods with different SNR (5 dB, 0 dB, –5 dB), where each column represents the different SNR and each row represents the imaging results of different methods at a specific SNR. The experiment results are obtained by MATLAB software on a personal computer with an Inter Core i7 3.8 GHz processor and 64 GB memory. It can be seen from Fig. 7 that the proposed method still has good performance even under low SNR conditions. As a result,the above-mentioned experiments verify the effectiveness of the proposed method.

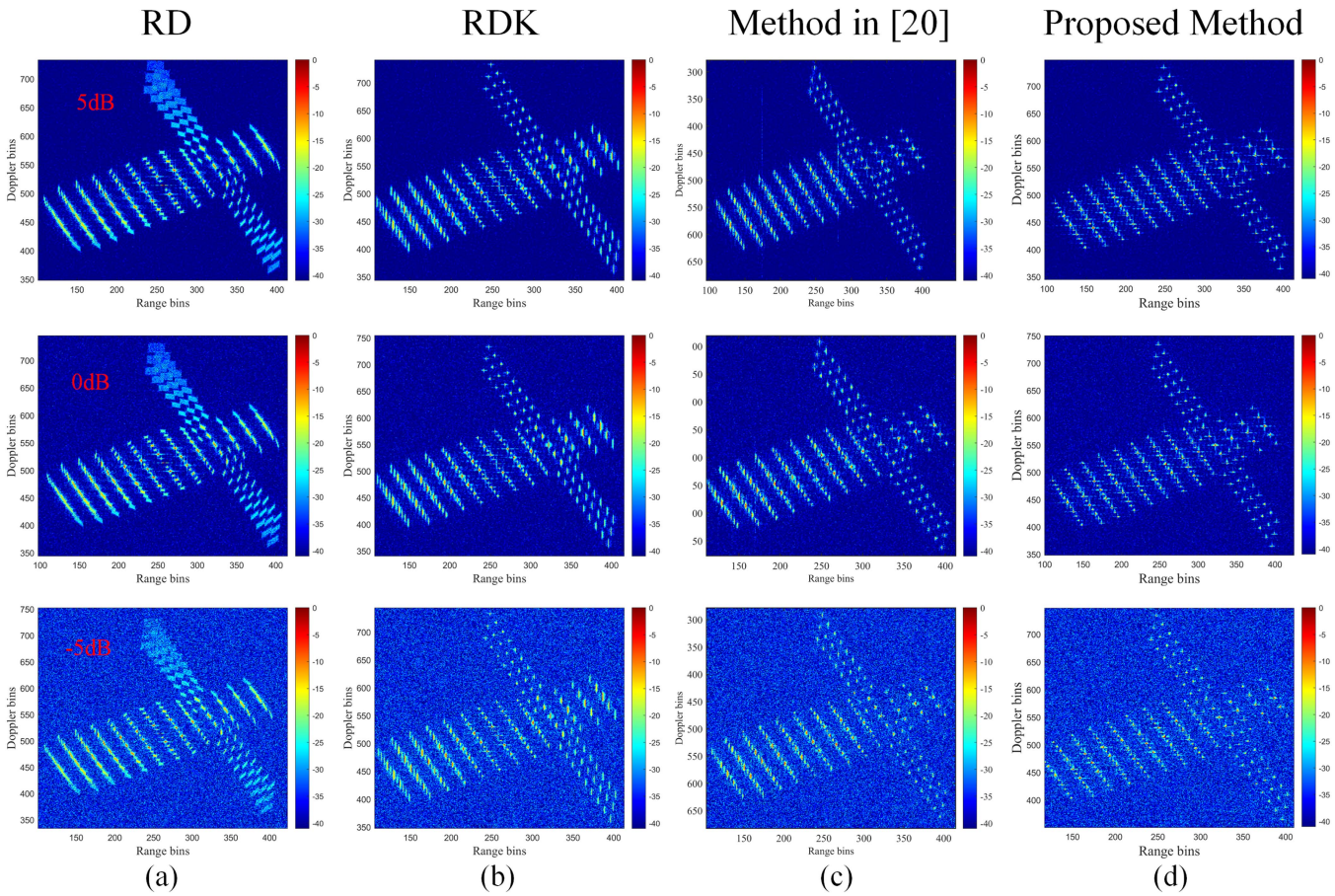

Fig. 7. Experimental results obtained by the four algorithms at different SNRs.

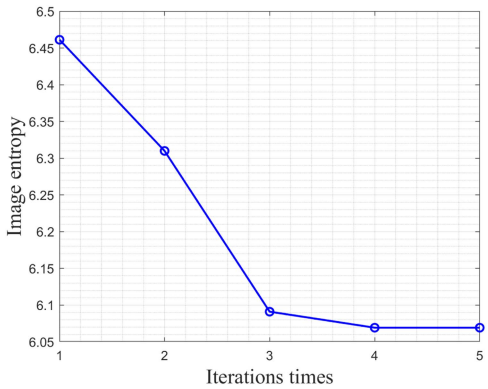

Fig. 8. Entropy against iteration times.

C. Discussion

Using SBISAR to image OS can overcome many disadvantages of ground-based ISAR imaging, such as the inability to observe GEO targets and atmospheric attenuation. However, limited by the requirement of miniaturization and low power, SBISAR needs to image OS within close distance. Therefore, OS moves slowly relative to SBISAR. Problems arise that are different from traditional ISAR high-resolution imaging when imaging OS.

First, OS will not maneuver significantly in most cases due to the constraints of orbital dynamics. In particular, communication and remote-sensing satellites need to maintain their posture stability when working in orbit. Thus, OS will not maneuver significantly when working generally in orbit, which differs from traditional ISAR imaging targets, such as ships and aircraft. Second, different from conventional ISAR imaging, the SBISAR antenna needs to point to the OS continuously, and the unit vector of LOS is time-varying due to the long CPI. Finally, the OS on-orbit will rotate nonuniformly to SBISAR, increasing the difficulty of high-resolution imaging.

Based on the orbital parameters in Table I and the derivation of the SBISAR echoes model, the higher order components of the null phase error need to be considered after calculating. A correction method of spatial variant phase errors in the SBISAR high-resolution imaging is proposed by combining the minimum entropy and the quasi-Newton method. In addition, a coarse estimation method of the motion parameters is proposed to accelerate the convergence of the quasi-Newtonian method by utilizing the orbital geometry relationship between SBISAR and OS and radar measurement techniques. Simulation experiments show that the proposed method has great advantages.

Two issues need to be studied. One is that if the OS receives an orbit change command or fails during observation by SBISAR, the motion of the OS relative to SBISAR will be more violent, especially the target's pitch, roll, and yaw rotation. The unit

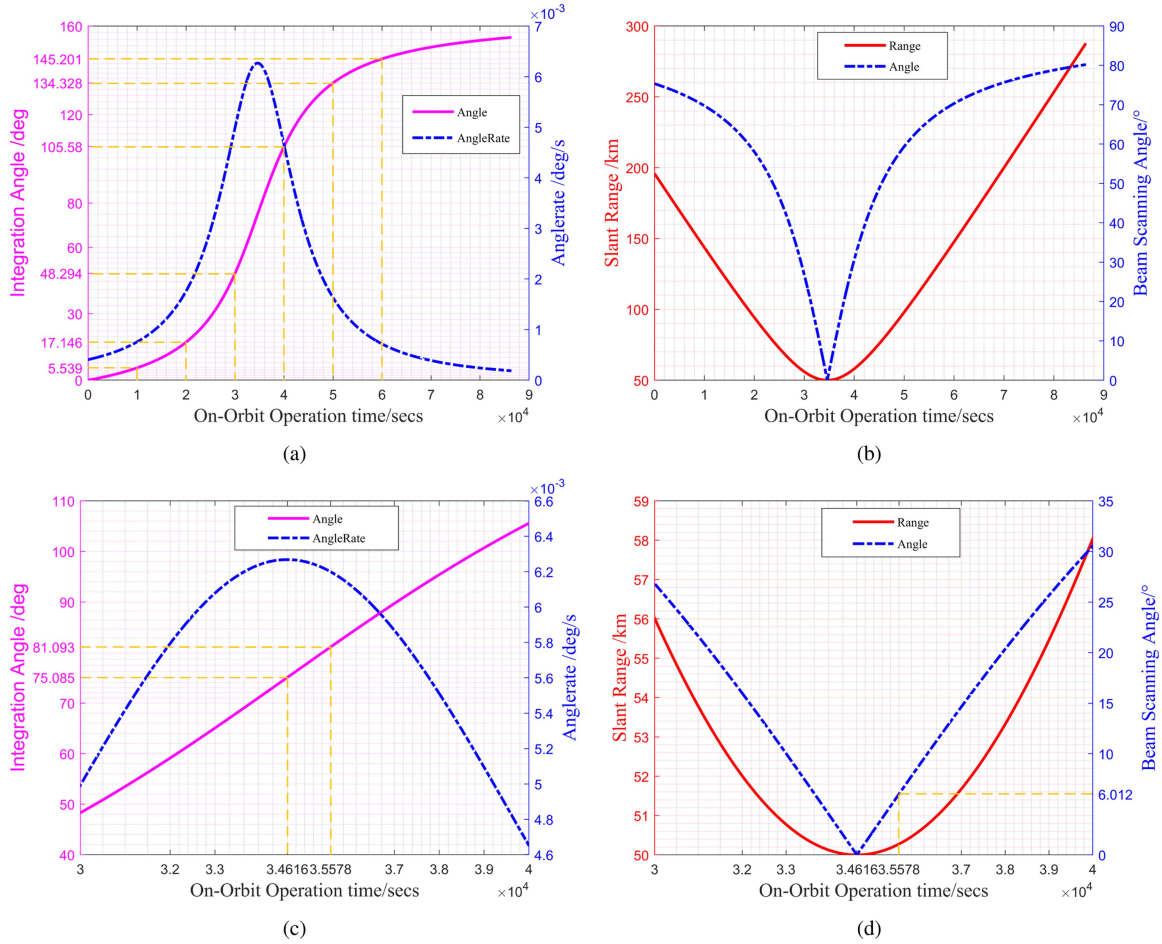

Fig. 9. Schematic diagram of changes in integration angle and slant range over operation time. (a) Relationship between the integration angle and the on-orbit operation time. (b) Relationship between the slant range and the on-orbit operation time. (c) Relationship between the integration angle and the on-orbit operation time in the optional imaging time periods. (d) Relationship between the slant range and the on-orbit operation time in the optional imaging time periods.

vector of LOS will also change. High-resolution imaging in this situation is difficult to achieve. The other is that SBISAR has a long CPI for OS imaging, so a solution needs to be found to achieve high-precision OS tracking by SBISAR. Research on the above-mentioned issues will be carried out in the future.

V. Conclusion

In this article, an processing method aims to compensate for 2-D spatial variant phase errors in high-resolution imaging of the OS by SBISAR is proposed. First, considering the kinematic characteristics of the OS on-orbit with SBISAR, the optimal imaging period is of the OS is analyzed, and the geometric model of SBISAR imaging of the OS is established. Second, the signal model for imaging the OS of SBISAR is formulated and the terms of 2-D spatial variant phase errors are derived. Furthermore, a parameterized minimum entropy method is proposed which integrates L-BFGS with IE as the objective function to estimate the parameters of spatial variant phase errors. Third, quasi-Newton's method exhibits local convergence. It is necessary for the initial values used in the iterative process to be in close proximity to the problem's solution. In addition, in the SBISAR imaging scene of the GEO target, the 2-D spatial variant phase error coefficients are required to be extremely small, which puts higher requirements on the initial value selection. Therefore, a new estimation method is proposed to obtain accurate initial values. The well-focused SBISAR images can be obtained after compensating spatial various phase errors. Finally, the effectiveness of the proposed method is verified with simulation data, and well-focused SBISAR images can be obtained.

Appendix A

Due to the limitation of the beam scanning range and slant range, not all moments during the on-orbit operation of SBISAR can be used to image GEO satellite. Therefore, it is imperative to engage in a discussion regarding the most advantageous timing for on-orbit imaging of SBISAR.

Fig. 9(a) shows the relationship between the integration angle and the on-orbit operation time. In particular, SBISAR observes satellite at 50 km below GEO. Although the Ka-band is used for the carrier frequency band, the integration angle should be greater than 6° to achieve 5 cm azimuth resolution. Assuming that the beam scanning range can reach ±15°. From Fig. 9(a), there are a very large number of optional imaging time periods

that satisfy the requirements of azimuth resolution condition. It should be emphasized that the very slow motion of the GEO satellite relative to SBISAR, even in Ka-band, results in a long CPI. Fig. 9(b) shows the beam scanning angle and slant range with respect to on-orbit operation time. Subject to minimizing the slant range and CPI, the optimal time period for imaging with the SBISAR is when the GEO satellite is directly above. The rate of integration angle is the largest at that moment, which can lead to the smallest CPI of 962 s, as shown in Fig. 9(c). In addition, the slant range between the GEO satellite and the SBISAR is minimized, and the beam scanning angle only needs to be greater than 6°, as shown in Fig. 9(d), which also satisfied the previous assumptions.

The LOS of SBISAR is determined by the elevation angle φ in the satellite body coordinate system. In contrast to traditional ISAR imaging, the CPI for GEO satellite is too long and the elevation angle φ varies within the CPI. Fig. 9(c) illustrates the anglerate of φ during the CPI, which can be accurately represented by a second-order polynomial function, given by

$$\varphi\left(t_m\right)=\varphi_0+\omega_\varphi t_m+\frac{\dot{\omega}_\varphi}{2}t_m^2 \tag{40}$$

where t_m is slow time, ω_φ and $\dot{\omega}_\varphi$ denote the rotational velocity and rotational acceleration, respectively. The motion of the satellite along its orbit, with only pitch rotation relative to the SBISAR, given by

$$\theta_p\left(t_m\right)=\omega_p t_m \tag{41}$$

where ω_p is the angular velocity of the GEO satellite.

Appendix B

Based on the second-order Taylor polynomial approximation, the (8) can be rewritten as

$$\mathbf{i}_{\text{los}}=\begin{bmatrix}-\varphi\left(t_m\right) & 0 & \frac{1}{2}\varphi^2\left(t_m\right)-1\end{bmatrix} \tag{42}$$

and (9) can be rewritten as

$$\mathbf{M}_{\text{rot}}\left(t_m\right)=\begin{bmatrix}1-\frac{1}{2}\theta_p^2\left(t_m\right) & 0 & \theta_p\left(t_m\right)\\ 0 & 1 & 0\\ -\theta_p\left(t_m\right) & 0 & 1-\frac{1}{2}\theta_p^2\left(t_m\right)\end{bmatrix} \tag{43}$$

the (11) can be obtained by substituting (42) and (43) into (15), and the parameters of t_m are given by

$$\begin{aligned}
K_0=&-x_p\left(1-\frac{\varphi_0^2}{2}\right)+z_p\varphi_0\\
K_1=&\,x_p\left(\varphi_0\omega_\varphi-\varphi_0\omega_p\right)+z_p\left[\omega_\varphi-\omega_p\left(1-\frac{\varphi_0^2}{2}\right)\right]\\
K_2=&-x_p\left[\omega_\varphi\omega_p+\left(-\frac{\dot{\omega}_\varphi\varphi_0}{2}-\frac{\omega_\varphi^2}{2}-\frac{\omega_p^2}{2}+\frac{\varphi_0^2\omega_p^2}{4}\right)\right]\\
&+z_p\left[\varphi_0\omega_\varphi\omega_p+\left(\frac{\omega_p}{2}-\frac{\varphi_0\omega_p^2}{2}\right)\right]\\
K_3=&-x_p\left[\frac{\dot{\omega}_\varphi\omega_p}{2}+\left(-\frac{\omega_p\omega_\varphi}{2}+\frac{1}{2}\varphi_0\omega_\varphi\omega_p^2\right)\right]\\
&-z_p\left[\omega_p\left(-\frac{1}{2}\dot{\omega}_\varphi\varphi_0-\frac{\omega_\varphi^2}{2}\right)+\frac{\omega_\varphi\omega_p^2}{2}\right]\\
K_4=&\,x_p\left(\frac{\dot{\omega}_\varphi^2}{8}-\frac{\omega_\varphi\varphi_0\omega_p^2}{4}-\frac{\dot{\omega}_\varphi\omega_p\omega_\varphi}{2}-\frac{\omega_p^2\omega_\varphi^2}{4}\right)\\
&+z_p\left(\frac{\dot{\omega}_\varphi^2}{8}-\frac{\dot{\omega}_\varphi\varphi_0\omega_p^2}{4}-\frac{\omega_p^2\omega_\varphi^2}{4}\right)\\
K_5=&-x_p\left(\frac{\dot{\omega}_\varphi^2\omega_p}{8}+\frac{\dot{\omega}_\varphi\omega_p^2\omega_\varphi}{4}\right)-z_p\frac{\dot{\omega}_\varphi\omega_p^2\omega_\varphi}{4}
\end{aligned} \tag{44}$$

$$K_6=-x_p\frac{\dot{\omega}_\varphi^2\omega_p^2}{16}-z_p\frac{\dot{\omega}_\varphi^2\omega_p^2}{16}. \tag{45}$$

According to (44), K_0 and K_1 can be expressed as

$$\begin{bmatrix}K_0\\K_1\end{bmatrix}=\mathbf{p}\begin{bmatrix}x_p\\z_p\end{bmatrix} \tag{46}$$

where

$$\mathbf{p}=\begin{bmatrix}\frac{\varphi_0^2}{2}-1 & \frac{\varphi_0^2}{2}-1\\ \omega_p-\frac{\varphi_0\omega_p}{2}+\varphi_0\omega_\varphi & \varphi_0\omega_\varphi-\varphi_0\omega_p\end{bmatrix}. \tag{47}$$

The coefficient of t_m^2 can be expressed as

$$K_2=\mathbf{q}\begin{bmatrix}x_p\\z_p\end{bmatrix} \tag{48}$$

where

$$\mathbf{q}=\begin{bmatrix}\frac{\dot{\omega}_\varphi\varphi_0}{2}+\frac{\omega_p^2}{2}-\frac{\varphi_0^2\omega_p^2}{4}-\varphi_0\omega_\varphi\omega_p+\frac{\omega_\varphi^2}{2}\\ \frac{\dot{\omega}_\varphi\varphi_0}{2}+\frac{\omega_p^2}{2}-\frac{\varphi_0^2\omega_p^2}{4}-\omega_\varphi\omega_p+\frac{\omega_\varphi^2}{2}\end{bmatrix}^T. \tag{49}$$

Similarly, the coefficients of t_m^3 can be expressed as

$$K_3=\mathbf{F}\begin{bmatrix}x_p\\z_p\end{bmatrix} \tag{50}$$

where

$$\mathbf{F}=\begin{bmatrix}-\frac{1}{2}\varphi_0\dot{\omega}_\varphi\omega_p+\frac{1}{2}\dot{\omega}_\varphi\omega_\varphi-\frac{1}{2}\varphi_0\omega_\varphi\omega_p^2-\frac{1}{2}\omega_p\omega_\varphi^2\\ -\frac{1}{2}\dot{\omega}_\varphi\omega_p+\frac{\omega_\varphi\dot{\omega}_\varphi}{2}-\frac{1}{2}\varphi_0\omega_\varphi\omega_p^2\end{bmatrix}^T. \tag{51}$$

Notice that, if the matrix $\mathbf{q}$ is irreversible, the phase errors is not exhibit the 2-D spatial variability, when it can be compensated by method in [42]. Therefore, the (ζ_x,ζ_z) and (ξ_x,ξ_z) can be expressed as

$$\begin{bmatrix}\zeta_z\\\zeta_x\end{bmatrix}=\left[\mathbf{q}\mathbf{p}^{-1}\right]^T \tag{52}$$

and

$$\begin{bmatrix}\xi_z\\\xi_x\end{bmatrix}=\left[\mathbf{F}\mathbf{p}^{-1}\right]^T. \tag{53}$$

After DFT and IDFT, (19) can be expressed as

$$\tilde{g}(m;k)=\sigma_p\,\text{sinc}\left[\frac{2B}{c}\left(m-K_0\right)\right]\cdot\text{sinc}\left[\frac{2T_a}{\lambda}\left(k-K_1\right)\right] \tag{54}$$

where K_0 and K_1 represent the position of the scatterer in the image, and can be expressed as

$$K_0 = \frac{c}{2B} \cdot m$$
$$K_1 = \frac{\lambda}{2T_{\text{CPI}}} \cdot k. \tag{55}$$

Substituting (55) into (21), the complex image $g(m,k)$ can be rewritten as

$$g(m,k) = \frac{1}{N}\sum_{n=0}^{N-1} \exp\left[j2\pi\frac{kn}{N}\right] \cdot s_p(m,n) \cdot \exp\left[j\left(C_x m + C_z k\right) n^2\right] \cdot \exp\left[j\left(Q_x m + Q_z k\right) n^3\right] \tag{56}$$

where $C_x = -2\pi\zeta_x/T_a, C_z = -2\pi\zeta_z c/\lambda B, Q_x = -2\pi\xi_x/T_a$, and $Q_z = -2\pi\xi_z c/\lambda B$.

Similarly to (29), the difference between the partial derivatives is $\partial\tilde{g}(m,k;\Re)/\partial C_x$. Therefore, the expression for the partial derivatives of other parameters are given by

$$\frac{\partial\tilde{g}(m,k;\Re)}{\partial C_z} = \frac{1}{N}\sum_{n=0}^{N-1} \exp\left[j2\pi\frac{kn}{N}\right] \cdot s_p(m,n) \cdot \exp\left[-j\left(C_x m + C_z k\right) n^2\right] \cdot \exp\left[-j\left(Q_x m + Q_z k\right) n^3\right] \cdot \left(-jkn^2\right) \tag{57}$$

$$\frac{\partial\tilde{g}(m,k;\Re)}{\partial Q_x} = \frac{1}{N}\sum_{n=0}^{N-1} \exp\left[j2\pi\frac{kn}{N}\right] \cdot s_p(m,n) \cdot \exp\left[-j\left(C_x m + C_z k\right) n^2\right] \cdot \exp\left[-j\left(Q_x m + Q_z k\right) n^3\right] \cdot \left(-jmn^3\right) \tag{58}$$

$$\frac{\partial\tilde{g}(m,k;\Re)}{\partial Q_z} = \frac{1}{N}\sum_{n=0}^{N-1} \exp\left[j2\pi\frac{kn}{N}\right] \cdot s_p(m,n) \cdot \exp\left[-j\left(C_x m + C_z k\right) n^2\right] \cdot \exp\left[-j\left(Q_x m + Q_z k\right) n^3\right] \cdot \left(-jkn^3\right). \tag{59}$$

REFERENCES

[1] H. Yunpeng, L. Kebo, L. Yan'gang, and C. Lei, "Review on strategies of space-based optical space situational awareness," *J. Syst. Eng. Electron.*, vol. 32, no. 5, pp. 1152–1166, 2021.

[2] E. Marchetti, A. G. Stove, E. G. Hoare, M. Cherniakov, D. Blacknell, and M. Gashinova, "Space-based sub-THz ISAR for space situational awareness–concept and design," *IEEE Trans. Aerosp. Electron. Syst.*, vol. 58, no. 3, pp. 1558–1573, Jun. 2022.

[3] S. J. Davey, T. Bessell, B. Cheung, and M. Rutten, "Track before detect for space situation awareness," in *Proc. Int. Conf. Digit. Image Comput.: Techn. Appl.*, 2015, pp. 1–7.

[4] B. Jia, K. D. Pham, E. Blasch, D. Shen, Z. Wang, and G. Chen, "Cooperative space object tracking using space-based optical sensors via consensus-based filters," *IEEE Trans. Aerosp. Electron. Syst.*, vol. 52, no. 4, pp. 1908–1936, Aug. 2016.

[5] C. R. Benson, "Enhancing space situational awareness using passive radar from space based emitters of opportunity," in *Proc. Mil. Commun. Inf. Syst. Conf.*, 2014, pp. 1–5.

[6] L. Yang et al., "Integration of rotation estimation and high-order compensation for ultrahigh-resolution microwave photonic ISAR imagery," *IEEE Trans. Geosci. Remote Sens.*, vol. 59, no. 3, pp. 2095–2115, Mar. 2021.

[7] Z. Ding, S. Liu, Y. Li, P. You, and X. Zhou, "Parametric translational compensation for ISAR imaging based on cascaded subaperture integration with application to asteroid imaging," *IEEE Trans. Geosci. Remote Sens.*, vol. 60, 2022, Art. no. 5200617.

[8] R. Cao, Y. Wang, C. Yeh, Y. Zhang, and X. Lu, "A novel optimal time window determination approach for ISAR imaging of ship targets," *IEEE J. Sel. Topics Appl. Earth Observ. Remote Sens.*, vol. 15, pp. 3475–3503, 2022.

[9] R. Avent, J. Shelton, and P. Brown, "The ALCOR C-band imaging radar," *IEEE Antennas Propag. Mag.*, vol. 38, no. 3, pp. 16–27, Jun. 1996.

[10] W. W. Camp, J. T. Mayhan, and R. M. O'Donnell, "Wideband radar for ballistic missile defense and range-Doppler imaging of satellites," *Lincoln Lab. J.*, vol. 12, no. 2, pp. 267–280, 2000.

[11] D. Cerutti-Maori, J. Rosebrock, C. Carloni, M. Budoni, I. Maouloud, and J. Klare, "A novel high-precision observation mode for the tracking and imaging radar TIRA–principle and performance evaluation," in *Proc. 8th Eur. Conf. Space Debris*,2021, pp. 1–15.

[12] S. Shao, H. Liu, L. Zhang, P. Wang, and J. Wei, "Ultrawideband ISAR imaging of maneuvering targets with joint high-order motion compensation and azimuth scaling," *IEEE Trans. Geosci. Remote Sens.*, vol. 60, 2022, Art. no. 5214621.

[13] G. Xu, M.-D. Xing, L. Zhang, J. Duan, Q.-Q. Chen, and Z. Bao, "Sparse apertures ISAR imaging and scaling for maneuvering targets," *IEEE J. Sel. Topics Appl. Earth Observ. Remote Sens.*, vol. 7, no. 7, pp. 2942–2956, Jul. 2014.

[14] J. Zheng, T. Su, W. Zhu, and Q. H. Liu, "ISAR imaging of targets with complex motions based on the keystone time-chirp rate distribution," *IEEE Geosci. Remote Sens. Lett.*, vol. 11, no. 7, pp. 1275–1279, Jul. 2014.

[15] X. Bai, R. Tao, Z. Wang, and Y. Wang, "ISAR imaging of a ship target based on parameter estimation of multicomponent quadratic frequency-modulated signals," *IEEE Trans. Geosci. Remote Sens.*, vol. 52, no. 2, pp. 1418–1429, Feb. 2014.

[16] J. Ding, Y. Li, J. Wang, M. Li, and J. Wei, "Joint motion compensation and distortion correction for maneuvering target bistatic ISAR imaging based on parametric minimum entropy optimization," *IEEE Trans. Geosci. Remote Sens.*, vol. 60, 2022, Art. no. 5118919.

[17] Y. Wang and Y. Jiang, "Inverse synthetic aperture radar imaging of maneuvering target based on the product generalized cubic phase function," *IEEE Geosci. Remote Sens. Lett.*, vol. 8, no. 5, pp. 958–962, Sep. 2011.

[18] Y. Wang and Y. Lin, "ISAR imaging of non-uniformly rotating target via range-instantaneous-doppler-derivatives algorithm," *IEEE J. Sel. Topics Appl. Earth Observ. Remote Sens.*, vol. 7, no. 1, pp. 167–176, Jan. 2014.

[19] Z. Bao, C. Sun, and M. Xing, "Time-frequency approaches to ISAR imaging of maneuvering targets and their limitations," *IEEE Trans. Aerosp. Electron. Syst.*, vol. 37, no. 3, pp. 1091–1099, Jul. 2001.

[20] P. Huang, X.-G. Xia, M. Zhan, X. Liu, G. Liao, and X. Jiang, "ISAR imaging of a maneuvering target based on parameter estimation of multicomponent cubic phase signals," *IEEE Trans. Geosci. Remote Sens.*, vol. 60, pp. 1–18, 2022.

[21] J. Wang, L. Zhang, L. Du, D. Yang, and B. Chen, "Noise-robust motion compensation for aerial maneuvering target ISAR imaging by parametric minimum entropy optimization," *IEEE Trans. Geosci. Remote Sens.*, vol. 57, no. 7, pp. 4202–4217, Jul. 2019.

[22] Z. Yang, D. Li, X. Tan, H. Liu, L. Xu, and G. Liao, "An efficient ISAR imaging approach for highly maneuvering targets based on subarray averaging and image entropy," *IEEE Trans. Geosci. Remote Sens.*, vol. 60, 2022, Art. no. 5102113.

[23] V. C. Chen and W. Miceli, "Time-varying spectral analysis for radar imaging of manoeuvring targets," *IEE Proc.-Radar Sonar Navigation*, vol. 145, no. 5, pp. 262–268, 1998.

[24] K.-T. Kim, I.-S. Choi, and H.-T. Kim, "Efficient radar target classification using adaptive joint time-frequency processing," *IEEE Trans. Antennas Propag.*, vol. 48, no. 12, pp. 1789–1801, Dec. 2000.

[25] R. Wang and Y.-C. Jiang, "ISAR ship imaging based on reassigned smoothed pseudo Wigner-Ville distribution," in *Proc. Int. Conf. Multimedia Technol.*, 2010, pp. 1–3.

[26] Z. Li et al., "Hybrid SAR-ISAR image formation via joint FrFT-WVD processing for BFSAR ship target high-resolution imaging," *IEEE Trans. Geosci. Remote Sens.*, vol. 60, 2022, Art. no. 5215713.

[27] C. Zhu, R. H. Byrd, P. Lu, and J. Nocedal, "Algorithm 778: L-BFGS-B: Fortran subroutines for large-scale bound-constrained optimization," *ACM Trans. Math. Softw.*, vol. 23, no. 4, pp. 550–560, Dec. 1997, doi: 10.1145/279232.279236.
[28] O. Montenbruck, E. Gill, and F. Lutze, "Satellite orbits: Models, methods, and applications," *Appl. Mech. Rev.*, vol. 55, no. 2, pp. B27–B28, 2002.
[29] C.-C. Chen and H. C. Andrews, "Target-motion-induced radar imaging," *IEEE Trans. Aerosp. Electron. Syst.*, vol. AES-16, no. 1, pp. 2–14, Jan. 1980.
[30] V. C. Chen and R. Lipps, "ISAR imaging of small craft with roll, pitch and yaw analysis," in *Proc. Rec. IEEE Int. Radar Conf.*, 2000, pp. 493–498.
[31] J. Li, H. Ling, and V. Chen, "An algorithm to detect the presence of 3D target motion from ISAR data," *Multidimensional Syst. Signal Process.*, vol. 14, no. 1/3, pp. 223–240, 2003.
[32] Z. Li et al., "A modified equivalent range model and wavenumber-domain imaging approach for high-resolution-high-squint SAR with curved trajectory," *IEEE Trans. Geosci. Remote Sens.*, vol. 55, no. 7, pp. 3721–3734, Jul. 2017.
[33] D. Wahl, P. Eichel, D. Ghiglia, and C. Jakowatz, "Phase gradient autofocus-a robust tool for high resolution SAR phase correction," *IEEE Trans. Aerosp. Electron. Syst.*, vol. 30, no. 3, pp. 827–835, Jul. 1994.
[34] S. Yang, S. Li, H. Fan, and H. Li, "An effective translational motion compensation approach for high-resolution ISAR imaging with time-varying amplitude," *IEEE Geosci. Remote Sens. Lett.*, vol. 20, 2023, Art. no. 4007805.
[35] S. Shao, L. Zhang, H. Liu, and Y. Zhou, "Accelerated translational motion compensation with contrast maximisation optimisation algorithm for inverse synthetic aperture radar imaging," *IET Radar, Sonar Navig.*, vol. 13, no. 2, pp. 316–325, 2019.
[36] J. Wang and D. Kasilingam, "Global range alignment for ISAR," *IEEE Trans. Aerosp. Electron. Syst.*, vol. 39, no. 1, pp. 351–357, Jan. 2003.
[37] P. Huang, G. Liao, Z. Yang, X.-G. Xia, J. Ma, and J. Zheng, "Ground maneuvering target imaging and high-order motion parameter estimation based on second-order keystone and generalized hough-HAF transform," *IEEE Trans. Geosci. Remote Sens.*, vol. 55, no. 1, pp. 320–335, Jan. 2017.
[38] L. Xi, L. Guosui, and J. Ni, "Autofocusing of ISAR images based on entropy minimization," *IEEE Trans. Aerosp. Electron. Syst.*, vol. 35, no. 4, pp. 1240–1252, Oct. 1999.
[39] L. Liu, F. Zhou, M. Tao, P. Sun, and Z. Zhang, "Adaptive translational motion compensation method for ISAR imaging under low SNR based on particle swarm optimization," *IEEE J. Sel. Topics Appl. Earth Observ. Remote Sens.*, vol. 8, no. 11, pp. 5146–5157, Nov. 2015.
[40] M. Dorigo, V. Maniezzo, and A. Colorni, "Ant system: Optimization by a colony of cooperating agents," *IEEE Trans. Syst., Man, Cybern., Part B. (Cybern.)*, vol. 26, no. 1, pp. 29–41, Feb. 1996.
[41] M. Richards, M. A Richards, J. A. Scheer, and W. A. Holm, "Principles of modern radar: Basic principles," Institution of Engineering and Technology, 2010.
[42] D. Zhu, L. Wang, Y. Yu, Q. Tao, and Z. Zhu, "Robust ISAR range alignment via minimizing the entropy of the average range profile," *IEEE Geosci. Remote Sens. Lett.*, vol. 6, no. 2, pp. 204–208, Apr. 2009.

Yifei Liu was born in Hebei, China, in 1999. He received the B.S. degree in electronic information engineering from Harbin Engineering University, Harbin, China, in 2020. He is currently working toward the Ph.D. degree in communication and information system with the Department of Space Microwave Remote Sensing System, Aerospace Information Research Institute, Chinese Academy of Sciences, Beijing, China.

He is currently with the University of Chinese Academy of Sciences, Beijing, China. His research interests include space-borne inverse synthetic aperture radar imaging and signal processing.

Weidong Yu (Member, IEEE) received the M.Sc. and Ph.D. degrees in electrical engineering from the Nanjing University of Aeronautics and Astronautics, Nanjing, China, in 1994 and 1997, respectively.

Since 1997, he has been with the Institute of Electronics, Chinese Academy of Sciences, now the Aerospace Information Research Institute, Beijing, China. He has been the Professor and Chief Designer for several synthetic aperture radar systems. His research interests include spacebore SAR implementation and SAR signal processing.

Shenghui Yang was born in Shandong, China, in 1997. He received the B.S. degree in electronic information engineering from the Harbin Institute of Technology, Weihai, China, in 2019. He is currently working toward the Ph.D. degree in communication and information with the Department of Space Microwave Remote Sensing System, Aerospace Information Research Institute, Chinese Academy of Sciences, Beijing, China.

He is currently with the University of Chinese Academy of Sciences, Beijing, China. His research interests include inverse synthetic aperture radar imaging and signal processing.

Shiqiang Li was born in Hebei, China, in 1967. He received the B.S. degree from the Beijing Institute of Technology, Beijing, China, in 1989, and the M.Sc. and Ph.D. degrees in electronic information from the Institute of China Electronics Technology Group and the Institute of Electronics, Chinese Academy of Sciences, Beijing, China, in 1992 and 2004, respectively.

He is currently a Professor with the Aerospace Information Research Institute, Chinese Academy of Sciences. His research interests include high resolution and wide-swath spaceborne SAR system design and simulation, and multistatic spaceborne SAR system.